scatterer. From these approximate force and moment time series, equation 17 of Spudich and Miller (1990) can then be used to calculate predicted data for each earthquake. This predicted data is subtracted from the observed data to form an unpredicted residual. The next iteration consists of repeating the above process with the unpredicted residual seismogram to generate an update to the force and moment time series for each scatterer. It is important to note that by using Olson's procedure, we obtain the same solution that would be obtained from a singular-value decomposition, namely the minimum-norm least-squares solution to the linear forward problem, retaining a prescribed range of eigenvalues. Of course, the real earthquake sources have radiation patterns that cause polarity changes; we have obtained mechanisms for all our events and the Q_i term (Spudich and Miller, 1990, equation 16) flips the data polarity when needed. We have compensated for the differing magnitudes of the earthquakes by normalizing all seismograms recorded at a particular station to a unit r.m.s. value.

Our paper differs from Spudich and Miller (1990) in several ways, most importantly in the number of scatterers used, the wave typed used, the conditions controlling the initiation and cessation of each scatterer, and the use of ray spreading. Spudich and Miller used only one trial scatterer, local at the seismic station. The force and moment time series derived for this scatterer were used to model the site effect at the station. In this paper we use a grid of scatterers (among which is one near the station, still used to model the site-effect). Spudich and Miller used both P and S body waves between the earthquake and the scatterer, while in this work we concentrate on the horizontal motions and allow only S body waves between the earthquakes and scatterers. (We have done several tests allowing both P and S body waves, and we have found that the P contribution to scattering was negligible.) We use causality to set the initiation and cessation times of each scatterer's time series; a scatterer cannot act so early that its scattered waves arrive at the station before the data initiate, and a scatterer does not act so late that its scattered waves arrive at the station after the data seismograms end. The use of causality also defines the relevant crustal volume to fill with trial scatterers. We have ignored ray spreading in calculating the ray amplitudes (i.e., we have set S^p and S^s equal to unity in Spudich and Miller equations 7 and 8). We did this because these terms become very large for buried scatterers located very near the earthquakes. This approximation does not affect any of the main results of this paper. In this paper we have also modified the elements of the A matrix in equation 25 of Spudich and Miller (1990). If a_{ij} is the ij-th element of **A**, then in this work we set $a_{ij} = sign(a_{ij}) = \pm 1$. This was done because too many seismograms from our already rather sparse data set were being downweighted by radiation pattern nodes. In addition, our suppression of radiation patterns compensates for the undesirable tendency of the minimum-norm solution to have power peaks at the loci of radiation pattern maxima. Various tests (not shown) show that this modification improves the reliability of the results when there are only a few tens of seismograms in the data set.

3.1 Comparison with other methods

The method used in this paper can be related to the theory of linearized scattering. In a very useful paper Tarantola (1984) related heterogeneities in material properties to perturbations in seismograms. Considering only the density term, for simplicity, his equation 4.7 shows how a localized perturbation in density $\delta\rho$ at point $\mathbf{x}$ in a volume V caused perturbations $\Delta u_i(\mathbf{x}_R, t)$ in the i-component of displacement u at receiver location $\mathbf{x}_R$ and time t,

$$\Delta u_i(\mathbf{x}_R, t) = -\int_V dV(\mathbf{x}) \dot{G}_{ij}(\mathbf{x}, t\,;\, \mathbf{x}_R, 0) * \dot{u}_j(\mathbf{x}, t) \delta\rho(\mathbf{x})$$

where $\dot{G}_{ij}(\mathbf{x}, t; \mathbf{x}_R, 0)$ is the time derivative of the i-component of displacement at $\mathbf{x}$ and t caused by a point impulse in the j direction at point $\mathbf{x}_R$ and time 0. $\dot{u}_j(\mathbf{x}, t)$ is the j component of velocity at $\mathbf{x}$ and t in the reference earth model, the asterisk denotes temporal convolution, and sums are taken over repeated indices. Again, for simplicity, assuming that the source is an instantaneous force at $\mathbf{x}_S$ given by

$$f_j(\mathbf{x}', t) = F_j \delta(\mathbf{x}' - \mathbf{x}_S)\delta(t)$$

we may combine this expression with Tarantola's equation 3.12 to obtain

$$\Delta u_i(\mathbf{x}_R, t) = -\int_V dV(\mathbf{x})\delta\rho(\mathbf{x})\dot{G}_{ij}(\mathbf{x}, t;\ \mathbf{x}_R, 0) * \dot{G}_{jk}(\mathbf{x}, t;\ \mathbf{x}_S, 0)F_k$$

The scattered wave field is related to a product of a Green's function describing propagation from the source to the scattering point x, a term expressing the strength of the scatterer, and another Green's function expressing propagation from the scatterer to the receiver.

The many attempts to map scatterers based on observed seismograms differ in the approximations they use for the Green's functions and the integral relations We use ray theory for propagation between the earthquake sources and the scattering points, and we treat the $\delta\rho(\mathbf{x})\dot{G}(\mathbf{x}, t)$ as an unknown secondary source terms that we try to determine. We assume that the unknown Green's function is causal, and we assume that the inner product between the two Green's functions has only a few low angular-order terms. We note parenthetically that our treatment of scatterers as secondary sources causes our method to be formally nearly identical to the technique that Frankel and Wennerberg (1989) used in an inversion of strong motion data for earthquake source dynamics. We also note that our treatment maintains the possibility of polarized, anisotropic scattering.

4. APPLICATION TO NORTH PALM SPRINGS AFTERSHOCKS

We have primarily analyzed a 2-dimensional grid of trial scatterers at the earth's surface. We used a grid of 16 x 16 trial scatterers having a 2 km separation in each dimension This grid exactly covers the study region shown in Figure 1. Various grid spacings were tried, and the 2 km spacing was the largest spacing that did not undersample the underlying solution. The seismic data used are shown in Spudich and Miller (1990). The approximate bandwidth of the data used is 2-4 Hz. The lower frequency is controlled by the natural period of the L-22 sensor. The upper frequency is the corner of a zero-phase Butterworth low-pass filter applied to the data. Because the stacking procedure requires phase coherence, the upper frequency limit of the analysis is controlled by the accuracy of the predicted travel time curves. A 4-Hz upper frequency means that we expect our predicted travel times are accurate to about 0.06 s. The filtered data were decimated to a 0.06 s sample interval. Because waves of a particular wavelength are most strongly scattered by heterogeneities having a comparable dimension, we expect our 3 Hz waves to be most strongly scattered by 1-km heterogeneities in the basement and $\sim$0.3 km heterogeneities in the sediments. As in Spudich and Miller (1990) , it was necessary to apply origin time corrections to the data to ensure phase coherence, and we used those determined in the previous work

Our first goal is to determine which scatters were strong (and presumably real). Consequently, for display purposes we reduced all the time series for a trial scatterer down to a single scalar proportional to the intensity of the scatterer. That scalar is the average power radiated by the scatterer, defined as follows. At each trial scatterer ξ we determined time series of duration T for each of the three components of the body force vector, $\dot{F}_i(\xi, t)$, i = 1, 2, and 3, and we determined 6 moment tensor time series, $\dot{M}'_{ij}(\xi, t)$. If we define the power in the $\dot{F}_i$ term to be

$$P_{F_i}(\xi) = \frac{1}{T}\int_0^T dt \left[\dot{F}_i(\xi, t)\right]^2$$

with a similar definition for power in the moment tensor terms, then we define the average power $P(\xi)$ to be

$$P(\xi) = P_{F_1}(\xi) + P_{F_2}(\xi) + \ldots + P_{M_{33}}(\xi)$$

Powers in the force and moment terms may be directly added because Spudich and Miller (1990) introduced a weighing in their definitions so that they have the same units. We have found the average power to be more stable

and more reliably interpreted than the individual force and moment and moment powers.

In Figure 4 we show the average power on the surface grid of scatterers and we show the effect of iterating the solution to improve data fit and decrease the solution norm. The data for each case are identical, 13.0 s of the north-south component of velocity recorded at SMP, with the data window containing early coda only, starting just after the S wave on the 23 recorded aftershocks. The power distribution for 1 iteration is the result obtained by simply stacking seismograms along the travel-time curves, as shown in Figure 3. The power distribution has a peak at the scatterer closest to station SMP. We expect a peak at the station because any near-station reverberations should stack coherently at the station, as shown in Figure 3. Consequently, the solution time series of the scatterer at (or nearest) the station models the direct S wave and the site reverberations. As we use progressively higher iterations, the peak at the station and a small secondary peak about 8 km west of the station become progressively sharper. Except where noted, for all subsequent results shown in this paper, 16 iterations are used, the ratio of largest to smallest eigenvalues retained in the solution is 50, and the power distributions are for a 13.0 s coda window following the direct S wave.

Because we always expect the direct S wave to produce a peak at the station, its peak is rather uninteresting and we have used a simple windowing scheme to remove the peak so as to make subsidiary peaks more prominent. Figure 5 shows the iterative inversion applied to the north-south component of ground velocity at SMP The power distribution for a 14.0 s duration window starting just before S shows a conspicuous peak at the station and a small subsidiary peak about 8 km west. A 1.0 s data window around the direct S pulse produces a sharp peak at the station, as expected. To examine the early coda, we analyzed the 13 s of data following the 1.0 s S window. The coda power distribution enhances the strong scatterer west of the station. A weak power peal remains at SMP. This probably represents the persistence of the site reverberations into the coda window. Except where noted in all of the following results we show power distributions in a 13.0 s window following the direct S wave

4.1 Correlation with geology

We interpret the coda power distributions for SMP EW and NS by superimposing them on the geologic map (Figure 6). Both power distributions consist of a broad region of elevated power about 15 km in diameter. This broad peak is seen in all our inversions, and shows that most of the energy in the early seismic coda comes from a region about 15 km in diameter (assuming surface scatterers). The cause of this peak can be understood simply from causality using Figure 3. Imagine that we are performing an inversion using only scatterers ξ_1, at the station, and ξ_2. Because of causality, waves scattered from ξ_2 cannot contribute to the data for times earlier than the dashed curve for ξ_2 and t_1. Consequently, all energy appearing in the seismograms earlier than that dashed curve can be radiated only from ξ_1 (or, in the case of many scatterers, from scatterers close to ξ_1).

The power distributions for both components of motion (Figure 6) show a peak at station SMP. This power peal represents energy that has reverberated unresolvably near the station. As shown in Figure 3, any near-station reverberation will add a coda to the direct S wave that will stack coherently over all earthquake seismograms

The interesting surprise, however, is the power peak 8 km WNW of SMP that falls at the contact of the alluvium with the older Pleistocene sedimentary deposits, which in this location are identified by Allen (1957) and Proctor (1968) as the Cabezon Fanglomerate. For brevity we will call this particular point on the edge of the fanglomerate point F, indicated on Figure 1. It should be noted that these fanglomerates are low-lying; the topographic edge of the valley lies 3 km further west at the contact with the upper Miocene unit. The power peak at F represents waves that travel as S waves from the aftershock hypocenters to the vicinity of point F and then travel by some unknown path to SMP. Apparently some scattering phenomenon associated with the edge of the alluvium and shape of the basement, rather than the topographic discontinuity at the edge of the valley, generates this scattered energy.

Like those for SMP, the coda power distributions for both components of SMC (Figure 7) show a broad mound about 15 km in diameter, indicating that the early coda energy is predominantly scattered from this 15 km wide region. In addition, the SMC distributions both show power peaks at the station, resulting from reverberations of energy very near the station. Unlike the SMP distributions, however, the SMC power distributions show no

conspicuous auxiliary power peak well separated from SMC. For both components of motion the main power peak is elongated along the strike of the Morongo Valley fault, and there is a power peak about 4 km southwest of SMC near the junction of the Morongo Valley fault and the Mission Creek fault. This secondary peak may correspond to either scattering from the southwest end of Morongo Valley or from scattering from the fault zone intersection, but we are not sure that the power peak is significant The main power peak at SMC is also elongated slightly northward, which may indicate scattered energy from the peninsula of Precambrian material jutting into the Morongo Valley, but this interpretation is extremely speculative.

4.2 The nature of the scattered waves

Because we have made no assumption about the mechanism of wave propagation between the scatterers and the station, our analysis procedure does not identify the type of waves propagating from *F* to SMP. While we might expect them to be scattered surface waves, based on previous studies in basins, we have done the following tests which show that laterally scattered S body waves are an important component. Although we could show the force and moment time series corresponding to the scatterer at *F*, they are uninformative. It is more informative to ask what motions the waves scattered from *F* generate at SMP. By answering this question, we will see what features in the data are modeled by waves scattered from *F*. This test is easy to perform since prediction of the expected motions is part of the iterative inversion procedure To do this we have run the inversion of the SMP-NS data again, but now we invert both the S wave and coda, and instead of using a 16 x 16 scatterer grid we use only two scatterers, one at the station and one at *F*. We have truncated the grid to two points because we believe that only the power peaks at the stations and at *F* are reliable. We have chosen to display observed and predicted seismograms for sets of 6 representative aftershocks distributed fairly uniformly over the aftershock volume (Figure 8).

Figure 9 shows that part of the energy scattered from *F* to SMP is a direct S body wave. The diamonds mark a conspicuous pulse that follows S at SMP, shown in a representative subset of the data Note that this pulse follows S by a variable amount, ranging from about 1 s for event 1941346 to about 2 s for event 1942351. The squares mark the initiation of the ground motions caused by scattering from *F* at the basin edge. Point *F* contributes a burst of energy that agrees quite well in arrival time with the observed later phase (diamond). It is important to note that the observed pulse (diamond) coincides with the beginning of the basin-edge time series because that enables us to identify its propagation mechanism; the initiation of the basin-edge time series travels via the minimum time path from the earthquake to the basin edge and then to the station, and thus the initial energy in the *F* time series must be an S body wave that travels directly from *F* to SMP by the fastest possible path, through the basement beneath the valley. The general time-coincidence of this phase and the observed pulses (diamonds) suggests that the observed pulses are scattered S waves.

Although the basin-edge contribution initiates with an S wave from *F* to SMP, we can demonstrate that the lower amplitude reverberative motions that follow the scattered *S* for several seconds in the *F* time series are real, although of unknown propagation mechanism. We divided the early coda at SMP into two non-overlapping windows, C1 and C2, shown in Figure 9 C1 is a 3-s-long window following the direct *S* window, and C2 is a 4-s-long window starting immediately after C1. Scattered energy from point *F* can be seen in the power distributions calculated form both of these coda windows (Figure 10), showing that the late, low amplitude reverberations in the basin-edge contribution are real. These waves traveled from the aftershocks to *F* as direct S body waves, and they traveled from *F* to SMP in some slower manner, possibly as surface waves or multiple-scattered body waves. Although we do not know their propagation mechanism, our procedure can use them to image the scatterer at *F*.

We cannot identify any obvious scattered waves in the SMC early coda other than waves scattered very near SMC and modeled by the scatterer at SMC. Figure 11 shows a two-scatterer decomposition of the observed SMC motions similar to that of Figure 9. In this case, one scatterer is located at SMC and the other is located at point M, at the southwest end of the Morongo Valley (Figure 1, 7), which is the location of the other major power peak. The solid circles in Figure 11 indicate a conspicuous phase following *S* in the data by about 1 s. Unlike the later phase at SMP, this later phase follows *S* by the same time interval in almost all seismograms. In the majority of observed seismograms this phase is modeled primarily by the scatterer at SMC, meaning that it is probably some sort of site reverberation. Squares mark the initiation of the contribution from *M*. Comparing 1960420, 1941815,

and 1940845, it is clear that the contributions from point *M* arrive at different times than the site reverberations (circles). There is no clear phase in the data that is being modeled by the scattered energy from *M*. Consequently, we do not know if the power peak at *M* represents any real scattered energy.

4.3 The vertical distribution of scatterers

We have performed preliminary investigations (not shown here) of the vertical distribution of scatterer power and we have found no evidence contradicting the hypothesis that the power peaks at SMC, SMP and *F* are confined to the top 3-4 km of the crust. If they extended to greater depth, we would probably observe this extension. We investigated the depth distribution of scatterers by running the inversion using single vertically dipping planes of scatterers striking either north-south or east-west and intersecting the Earth's surface wither at SMC, SMP and/or *F*. In these inversions, power peaks were found at the surface locations of SMC, SMP and *F*. These power peaks did not extend to depths greater than 4 km. While other power peaks were sometimes found at about 10 km depth, these deeper peals in general were smaller than those at the surface. While it is possible for us to run an inversion using a fully 3-dimensional grid of scatterers, we must do so cautiously because a 3-D inversion will make an already underdetermined problem even more underdetermined, and it will be more difficult to determine the significance of deeper power peaks.

5. DISCUSSION

The most important observations we have made are 1) assuming surface scattering, most of the energy in the early coda is scattered from a region within about 8 km of the seismic stations, 2) at both stations a substantial fraction of the energy in the early coda comes from scattering very near (within 2 km of) the station, 3) at SMP inside the Coachella Valley we have observed energy scattered from a particular place (point *F*) at the edge of the valley alluvium, 4) at SMP, the initial part of the scattered energy from *F* is an S body wave probably traveling through the basement beneath the valley, 5) the scattered energy from *F* continues for several seconds, indicating that multiple scattering and/or surface waves may be involved in its propagation, and 6) scattering at the basin edge *F* and at the stations appears to occur no deeper than 4 km.

Observation 3 suggests that three may be particular places at the edges of basins that are especially strong scatterers of incident seismic waves. We will call these places 'bright spots,' borrowing the term used in the exploration industry to describe highly reflective zones. We do not know the factors that cause strong scattering at a bright spot. Perhaps it is some combination of shape of the boundary, impedance contrast between the alluvium and basement, slope of the contact, frequency band, and scattering angle. We do not know which of these factors operates in our case.

There is ample theoretical evidence for nonuniform scattering from basin edges. In theoretical studies of SH waves vertically incident upon 2-dimensional basins, both Hill *et al.* (1990) and Papageorgiou and Kim (1991) have shown that the steeper edge of the basin is the stronger scatterer of surface waves into the basin. Horike *et al.* (1990), studying *S* vertically incident on three-dimensional basins, noted that the sides and corners of the basins preferentially generated scattered surface waves. Bard and Bouchon (1980a) noted preferential scattering of surface waves from basin edges nearer to the source, as did Frankel and Vidale (1992) in their three-dimensional simulations of waves in a realistic basin geometry. They noted several causes of surface waves propagating out of the direct source-receiver azimuth. In their simulations, basement outcrops and irregularities in the edge of the valley acted like point diffractors of surface waves. S waves incident non-normally on a edge (seen in map view) caused 'refraction' of the converted surface waves.

Several observational studies of nonuniform scattering from basin edges warrant special attention. Observing wave propagation directions at a seismograph array in the Santa Clara Valley of California, Frankel *et al.* (1991) noted substantial surface waves propagated in a westerly direction, different from the backazimuth to the microearthquake sources. They speculated that these surface waves may have scattered off the Santa Teresa Hills, a peninsula of basement protruding into the alluvium of the Santa Clara Valley, and off Oak Hill, a basement outcrop in the valley. They also noted some waves scattered from the west side of the valley, also at a backazimuth

different from the source. Some of these observed waves were simulated by Frankel and Vidale (1992), who speculated that the unmodeled waves might have been caused by scattering from a shallow basement horst. Phillips *et al.* (1993) found that Love waves observed on an array in the Kanto plain all appeared to come from a particular spot at the edge of the basin west of the array, regardless of the location of the earthquake source. This spot at the basin boundary was almost the closest boundary point to the array, and Phillips and his colleagues hypothesized that it was the spot's proximity to the array that made it the apparent location of scattering. Horike (1988) attributed scattered surface waves observed at array OGR in the Kyoto basin to conversion at the edge of the basin closest to the source, but his observations could also be interpreted as indicating waves scattering from a location on the basin edge about 2 km south of station OBK, which is almost the point on the basin edge closest to OGR. Gupta *et al.* (1990) noted scattering of teleseismic P to R_g at a steep topographic slope near the NORESS array, and noted that the scattering did not depend strongly on the incidence azimuth.

Taking all these observations together, we conclude that several processes are at work. First, our observations and Frankel's clearly support the 'bright spot' hypothesis, that there are scattering loci that are neither the closest basin edge to the source or to the observer. Horike's and Phillips' observations might also indicate the existence of a bright spot, but these bright spots are suspiciously close to the nearest basin edge. Second, as surface waves will no doubt be affected by the high attenuation in the shallow alluvium, it is likely that scattering from the closest edge to the receiver will be preferentially observed at any basin site. Third, scattering from the basin edge closest to the source is supported theoretically and also by Frankel *et al.* (1991)'s observation on their event 1 that Love waves having 5 s period appear to come from the basin edge toward the source. This is not surprising because the amplitude of the wave incident upon the basin will be highest near the source, and a basement contact dipping in the direction of S-wave propagation is especially effective in converting body waves to surface waves. A fourth factor may explain Frankel *et al.*'s observation of waves scattered from the west side of the valley If surface waves are generated uniformly at all points on a sinuous valley edge when illuminated by a propagating incident wave, then there will be points of stationary phase (as in Kirchhoff diffraction) that will appear to generate pulses at an observer Finally, the earthquake source mechanisms will cause some potential scattering loci to be illuminated more strongly than others. Some combination (determined by the amplitude of the illuminating energy) of these four factors will control the observed motions in particular situations.

Theoretical studies hint at the nature of the 2-4 Hz waves have observed to be scattered from F to SMP within the valley. We have already noted that the scattered waves initiate with a conspicuous S pulse, but continue for several seconds. This wave strongly resembles the phases D1 and E1 in the 3-D simulation of Horike *et al.* (1990), which they identify as upgoing body waves and surface waves. However, it is possible that both our S phase and their phase D1 may be S waves diffracted from the basin edge and refracted along the top of the basement. The latter energy we observed at SMP may also be higher mode surface waves, as observed in theoretical calculations by Bard and Bouchon (1980b), Horike *et al.* (1990) and by Frankel and Vidale (1992).

It is particularly puzzling that we observe scattering from point F, located at the contact between Cabezon Fanglomerate and alluvium, where the impedance contrast is probably small, and we can only speculate about the cause of this scattering. Probably the observed waves are not scattered from this impedance contrast, but are instead scattered from the alluvium-basement contact, which probably has a much greater impedance contrast. Matti *et al.* (1985) have mapped a normal fault about 3 km west of F, but the impedance contrast across this fault is probably smaller than the alluvium-basement contrast. Scattering mechanisms may exist, particularly for scattering from extended interfaces, so that the scattered waves appear to come from a different place than the geologic structure causing the scattering For example, Frankel and Vidale (1992) observed that a dipping alluvium-basement contact can convert incident S waves into trapped surface waves very efficiently. Because this conversion process does not happen exactly at the basement-alluvium contact but instead occurs as a multiple reflection phenomenon inside the basin, such converted waves may appear to originate within the basin. This explanation might explain why the delayed waves seen in time window C2 of Figure 9 appear to come from F, but it would not explain why the earliest arriving energy in window C1 appears to come from F. This energy must propagate almost entirely as a S wave in the basement to arrive at the time observed.

We hope that our work will improve seismologists' ability to predict ground motions at specific sites using

empirical Green's function (EGF) summations. Spatial interpolation of EGFs is almost always necessary for such summations, and accurate interpolation requires a knowledge of the types, time functions, and propagation directions *in the source volume* of the waves that constitute the EGFs. In fact, Figures 9 and 11 are examples of such an EGF interpolation; for each station we identified two strong sources of scattered energy and we estimated EGFs (the 'sum' traces) based on the presumed existence of these scatterers. In this paper we have not tried to optimize the accuracy of the interpolation, which is complicated by the underdetermined nature of the inversion (see Spudich and Miller, 1990, for details), but that is a future goal.

Our method will be most useful for EGF interpolation and simulation when the EGF sources are located in the source volume of the anticipated large event. The identification of bright spots may be affected by the set of earthquakes used (owing to their locations and radiation patterns), so if the EGFs and the anticipated large event share the same source volume and dominant mechanism, it is likely that a bright spot identified using the EGFs will probably also be bright in the main shock.

6. REFERENCES

Aki, K. (1988). Local site effects on strong ground motion, in *Earthquake Engineering and Soil Dynamics II* -- Recent advances in ground-motion evaluation, Geotechnical Special Publication, **20**, *Am. Soc. Civ. Eng.*, 103-155.

Aki, K. and P.G. Richards (1980). Quantitative Seismology: Theory and Methods, W.H. Freeman, New York.

Allen, C.R. (1957). The San Andreas fault zone in San Gorgonio Pass, southern California, *Geol. Soc. Am. Bull.*, **68**, 315-349.

Bannister, S C., E.S. Husebye and B.O. Ruud (1990). Teleseismic *P* coda analyzed by three-component and array techniques: deterministic location of topographic *P*-to-R_g scattering near the NORESS array, *Bull Seism. Soc. Am.*, **80**, 1969-1986.

Bard, P. and M. Bouchon (1980a). The seismic response of sediment filled valleys. Part I. The case of incident SH waves, *Bull. Seism. Soc. Am.*, **70**, 1263-1286

Bard, P. and M. Bouchon (1980b). The seismic response of sediment filled valleys. Part II The case of incident P and SV waves, *Bull. Seism. Soc. Am.*, **70**, 1921-1941.

Borcherdt, R.D., J.B. Fletcher, E.G. Jensen, G.L. Maxwell, J.R Vanshaack, R E. Warrick, E Cranswick, M.J S. Johnston and R. McClearn (1985). A General Earthquake Observation System (GEOS), *Bull. Seism. Soc. Am.*, **75**, 1783-1825.

Borcherdt, R., G. Glassmoyer, M. Andrews and E. Cranswick (1989) Effect of site conditions on ground motion and damage, *Earthquake Spectra*, special supplement *Armenia Earthquake Special Report*, 23-42.

Esteva, L., H. Krawinkler and J.M. Roesset (1989). Working group conclusions on response and performance of structures, in *Lessons Learned from the 1985 Mexico Earthquake*, ed. V.V Bertero, Earthquake Engineering Research Institute Publication, **89-02**, 84-87.

Frankel, A., S. Hough, P. Friberg and R. Busby (1991). Observations of Loma Prieta aftershocks from a dense array in Sunnyvale, California, *Bull. Seism. Soc. Am.*, **81**, 1900-1922.

Frankel, A. and J. Vidale (1992). A three-dimensional simulation of seismic waves in the Santa Clara Valley, California, from a Loma Prieta aftershock, *Bull. Seism. Soc. Am.*, **82**, 2045-2074.

Frankel, A. and L. Wennerberg (1989). Rupture process of the M_s 6 6 Superstition Hills, California, earthquake determined from strong-motion recordings: Application of tomographic source inversion, *Bull. Seism Soc. Am.*, **79**. 515-541

Gupta, I.N., C.S. Lynnes, T.W. McElfresh and R.A. Wagner (1990). *F-K* analysis of NORESS array and single-station data to identify sources of near-receiver and near-source scattering, *Bull. Seism. Soc. Am.*, **80**. 2227-2241.

Hanks, T C. (1975). Strong ground motion of the San Fernando, California, earthquake: Ground displacements, *Bull. Seism. Soc. Am.*, **65**, 193-225.

Hartzell, S. (1989). Comparison of waveform inversion results for the rupture history of a finite fault: Application to the 1986 North Palm Springs, California, earthquake, *J. Geophys. Res.*, **94**, 7515-7534

Hedlin, M.A.H , J.B. Minster and J A Orcutt (1911) Beam stack imaging using a small aperture array, *Geophys. Res. Lett.*, **18**, 1771-1774.

Harraiz, M. and A.F. Espinoza (1987). Coda waves: a review, *Pure Appl. Geophys* , **125**, 499-577.

Hill, J., H. Benz, M. Murphy and G. Schuster (1990) Propagation and resonance of SH waves in the Salt Lake Valley, Utah, *Bull. Seism. Soc Am.*, **80**, 23-42.

Hill, N.R and A.R. Levander (1984). Resonances of low-velocity layers with lateral variations, *Bull. Seism. Soc Am.*, **74**, 521-537

Horike, M. (1988) Analysis and simulation of seismic ground motions observed by an array in a sedimentary basin, *J. Phys. Earth*, **36**, 135-154.

Horike, M., H. Uebayashi and Y. Takeuchi (1990). Seismic response in three-dimensional sedimentary basin due to plane S wave incidence, *J. Phys. Earth*, **38**, 261-284.

Hutchings, L and F Wu (1990). Empirical Green's functions from small earthquakes: A waveform study of locally recorded aftershocks of the 1971 San Fernando earthquake, *J. Geophys. Res* , **95**, 1187-1214.

Jones, L M., K.L. Hutton, D D. Given and C.R. Allen (1986). The North Springs, California, earthquake sequence of July 1986, *Bull. Seism. Soc. Am.*, **76**, 1828-1843.

Key, F.A. (1967). Signal-generated noise recorded at the Eskdalemuir seismometer array station, *Bull. Seism. Soc Am* , **57**, 27-37.

Ley, T. (1987). Analysis of near-source contributions to early P-wave coda for underground explosions III. Inversion for isotropic scatterers, *Bull. Seism. Soc Am* , **77**, 1767-1783

Levander, A.R and N.R. Hill (1985) *P-SV* resonances in irregular low-velocity surface layers, *Bull. Seism. Soc Am.*, **75**, 847-864.

Liu, H.-L. and T. Heaton (1984) Array analysis of the ground velocities and accelerations from the 1971 San Fernando, California, earthquake, *Bull. Seism. Soc. Am.*, **74**, 1951-1968.

Lynnes, C.S. and T Lay (1989). Inversion of *P* coda for isotropic scatterers at the Yucca Flat Test Site, *Bull. Seism. Soc. Am.*, **79**, 790-804.

Matti, J.C., D.M. Morton and B.F. Cox (1985). Distribution and geologic relations of fault systems in

the vicinity of the Central Transverse Ranges, southern California, Open-File Report **85-365**, U.S Geological Survey.

Mori, J. and A Frankel (1990). Source parameters for small events associated with the 1986 North Palm Springs, California, earthquake determined using empirical Green's functions, *Bull. Seism. Soc. Am.*, **80**. 278-295.

Nikolaev, A.V. and P A. Troiskiy (1987). Lithospheric studies based on array analysis of *P*-coda and microseisms, *Tectonophysics*, **140**, 103-113

Nishigami, K. (1991). A new inversion method of coda waveforms to determine spatial distribution of coda scatterers in the crust and uppermost mantle, *Geophys. Res. Lett.*, **18**, 2225-2228.

Olson, A.H. (1987). A Chebyshchev condition for accelerating convergence of iterative tomographic methods: solving large least squares problems, *Phys. Earth Planet Interiors*, **47**, 333-345.

Papageorgiou, A. and J. Kim (1991). Study of the propagation and amplification of seismic waves in Caracas Valley with reference to the 29 July 1967 earthquake: SH waves, *Bull. Seism. Soc. Am.*, **81**, 2214-2233.

Phillips, W.S., S. Kinoshita and H. Fujiwara (1993). Basin-induced Love waves observed using the strong motion array at Fuchu, Japan, *Bull Seism. Soc. Am.*, **83**, 65-84.

Proctor, R.J. (1968). Geology of the Desert Hot Springs-Upper Coachella Valley area, California, Special Report 94, *Calif. Div. Mines and Geol.*

Scherbaum, F. (1987). Seismic imaging of site response using microearthquake recordings. Part II. Application to the Swabian Jura, southwest Germany, seismic network, *Bull. Seism Soc. Am.*, **77**, 1924-1944.

Spudich, P. and T. Bostwick (1987). Studies of the seismic coda using an earthquake cluster as a deeply buried seismograph array, *J. Geophys Res.*, **92**, 10,526-10,546.

Spudich, P. and D.P. Miller (1990). Seismic site effects and the spatial interpolation of earthquake seismograms: Results using aftershocks of the 1986 North Palm Springs, California, earthquakes, *Bull. Seism. Soc. Am.*, **80**, 1504-1532.

Tarantola, A (1984). The seismic reflection inverse problem, in *Inverse Problems of Acoustic and Elastic Waves*, eds. F Santosa, Y. Pao, W Symes and C. Holland, *Soc. Industr. Appl. Math.*, Philadelphia, 104-181.

Yamanaka, H , K. Seo and T Samano (1989). Effects of sedimentary layers on surface wave propagation, *Bull. Seism. Soc. Am.*, **79**, 631-644.

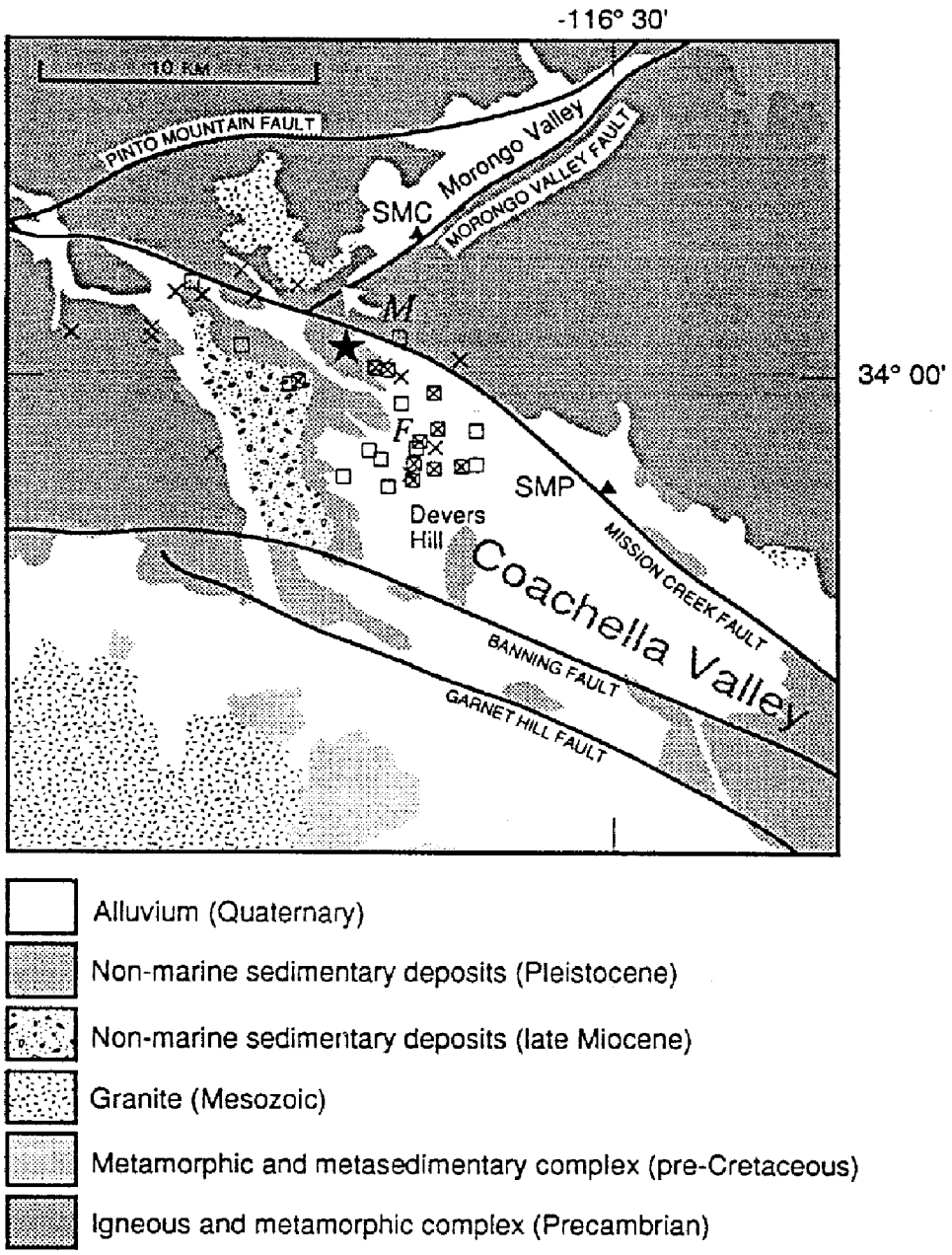

Fig. 1 Simplified geologic map of the North Palm Springs, California, study region, showing the seismic stations SMC and SMP used in this study. X's and squares show the aftershock epicenters recorded by SMC and SMP respectively. *F*, southeast of the main shock epicenter (star), is a locus of strong scattering, *M*, near SMC, may also be a locus of scattering.

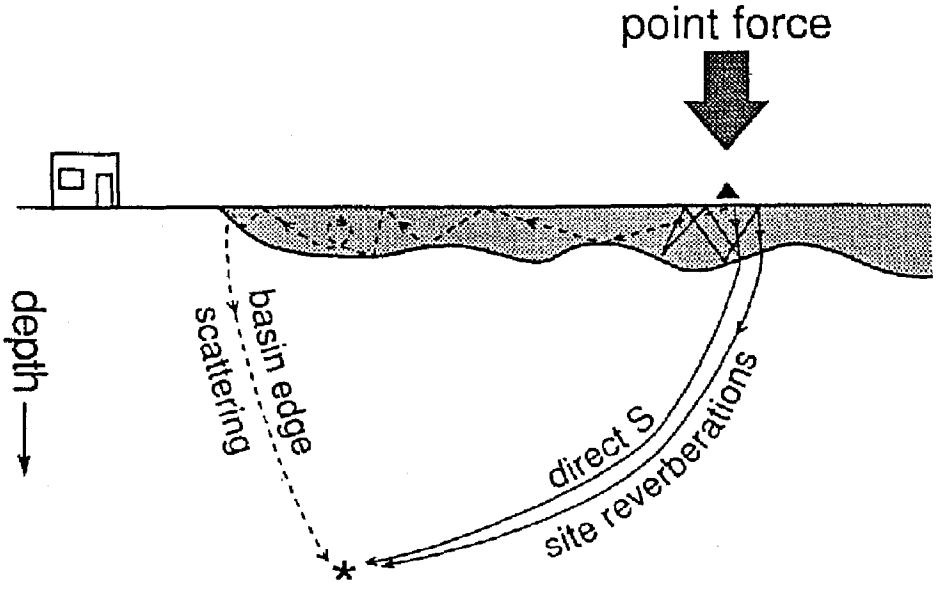

Fig. 2 A schematic seismic experiment in the reciprocal geometry. The cross-section shows an alluvial layer (gray) overlying a harder, uniform unit. An instantaneous point force is applied at the surface (triangle) and the motions are recorded at depth (asterisk). The solid lines show the ray paths of the direct S wave and one of the many rays reverberated beneath the force application site. The dashed line shows (schematically) a wave which propagates in some complicated fashion through the alluvium and converts into a downgoing S wave at the basin edge.

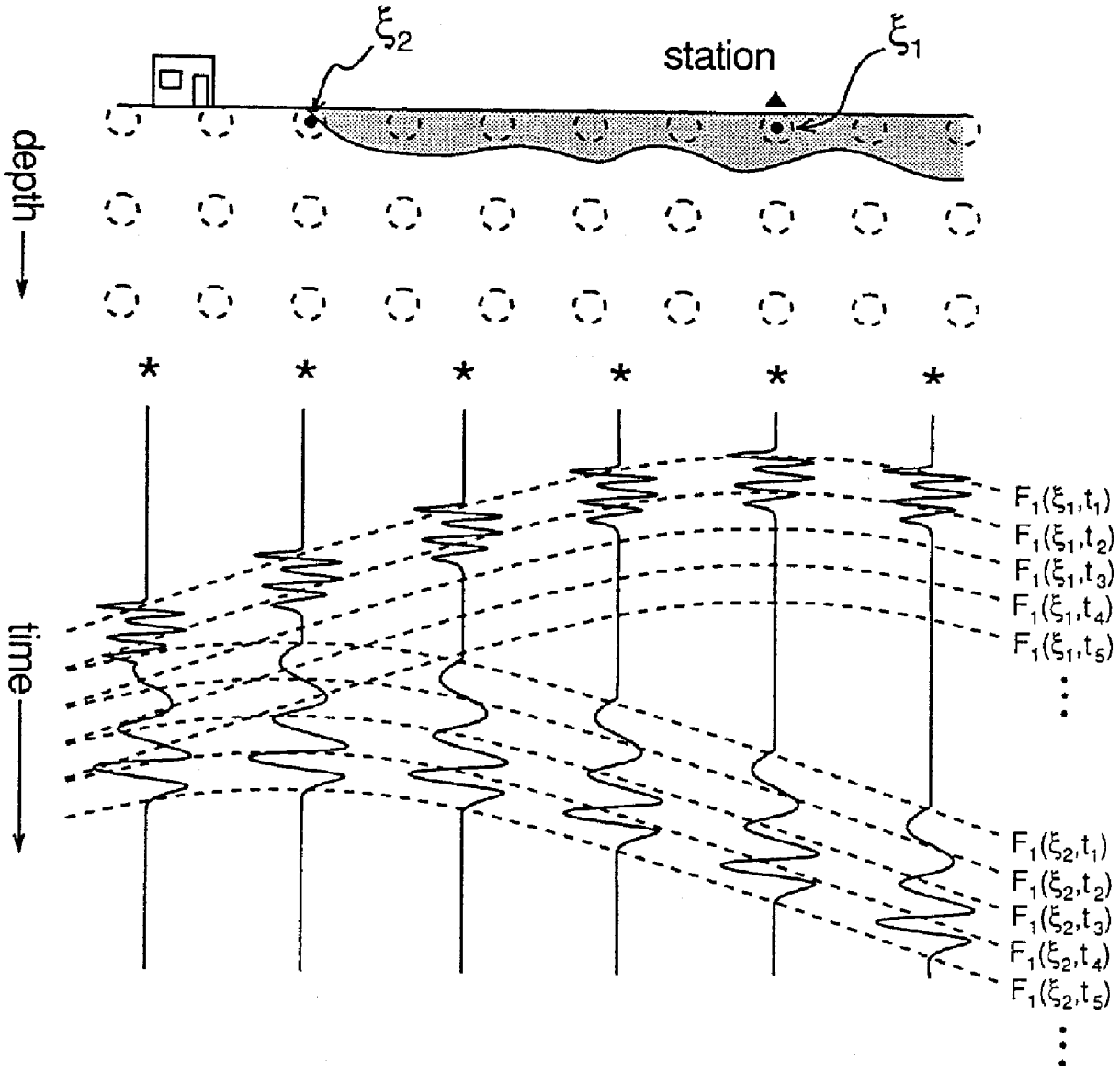

Fig. 3 Geometry and data from a schematic experiment. The geology is identical to that in Figure 2. Asterisks represent a horizontal line of microearthquake sources and the triangle is a seismograph. Beneath each earthquake is its associated seismogram. Dashed circles are trial scatterers, and solid circles are scatterers at the station and at the basin edge. The upper hyperbolic dashed lines are travel time curves for propagation between the scatterer at the station and the earthquakes (in a smooth reference medium), and the lower dashed lines are for propagation between the basin edge scatterer and the earthquakes. For scatterers 1 and 2, the dashed curves for t_1 are meant to indicate the earliest possible causal arrival times, corresponding to S wave propagation between station, scatterer and earthquake. Force and moment time series for each scatterer are assembled by stacking the seismograms along the appropriate set of curves.

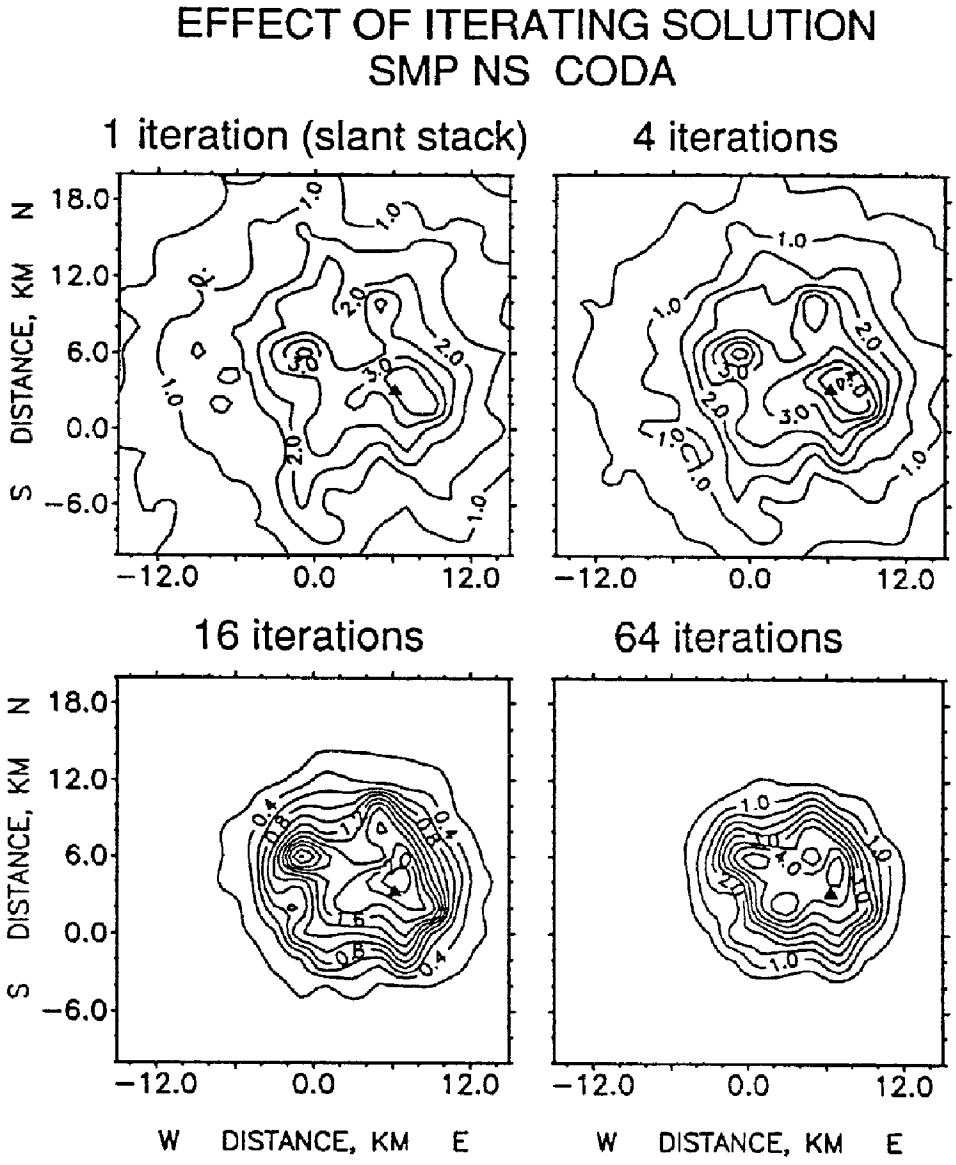

Fig. 4 Average power distributions for SMP north-south ground velocities, using a 13.0 s data window starting just after the direct S arrivals. The '1-iteration' panel shows the result of simple stacking of the seismograms with corrections for radiation patterns. Main and subsidiary peaks become sharper with more iterations. The triangle shows the location of SMP. Power units are arbitrary

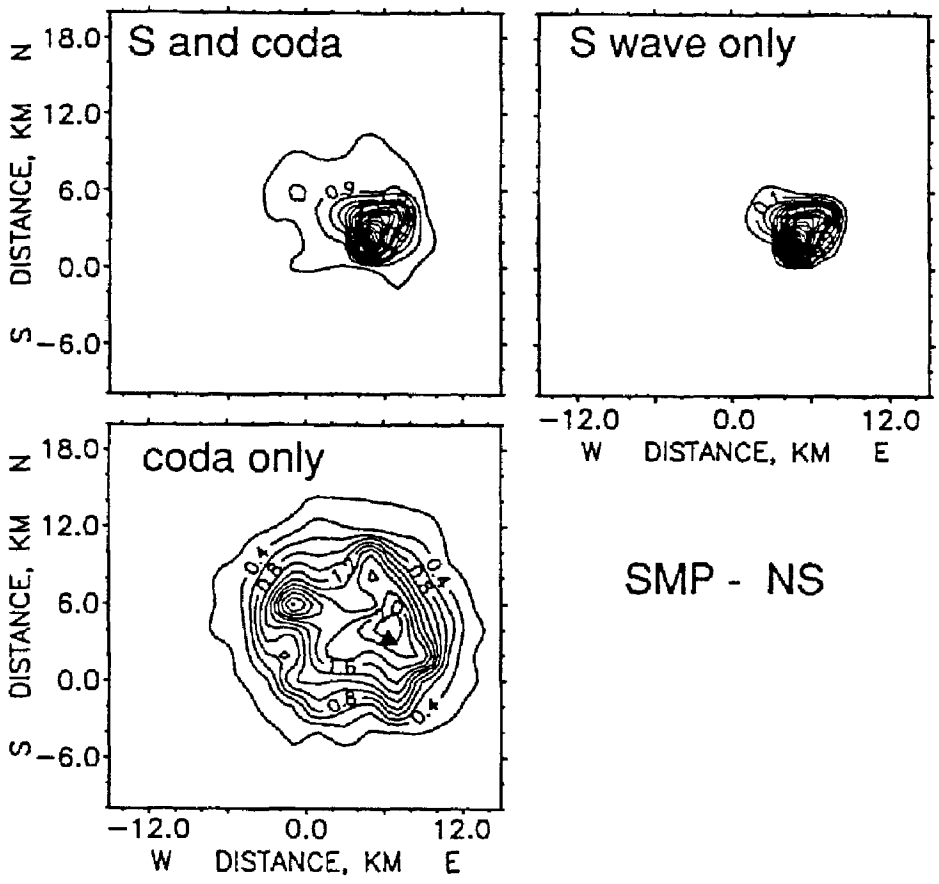

Fig. 5 Windowing of time series to accentuate scatterers contributing to the early coda. Each panel shows the average power distribution for the north-south component of ground velocity at SMP. The upper left panel is for a 14.0 s segment of data starting just before the direct S wave on each aftershock. The upper right window is for a 1.0 s window of data containing the direct S wave. The lower left window is for the 13 s of data following the direct S window. The power peak at the station (triangle) is caused primarily by the direct S wave. Analysis of the data window excluding the direct S wave accentuates scatterers away from the station. Power units are arbitrary. Contour interval is 0.05 of the maximum power in the upper panels and is 0.1 of the maximum power in the lower panel.

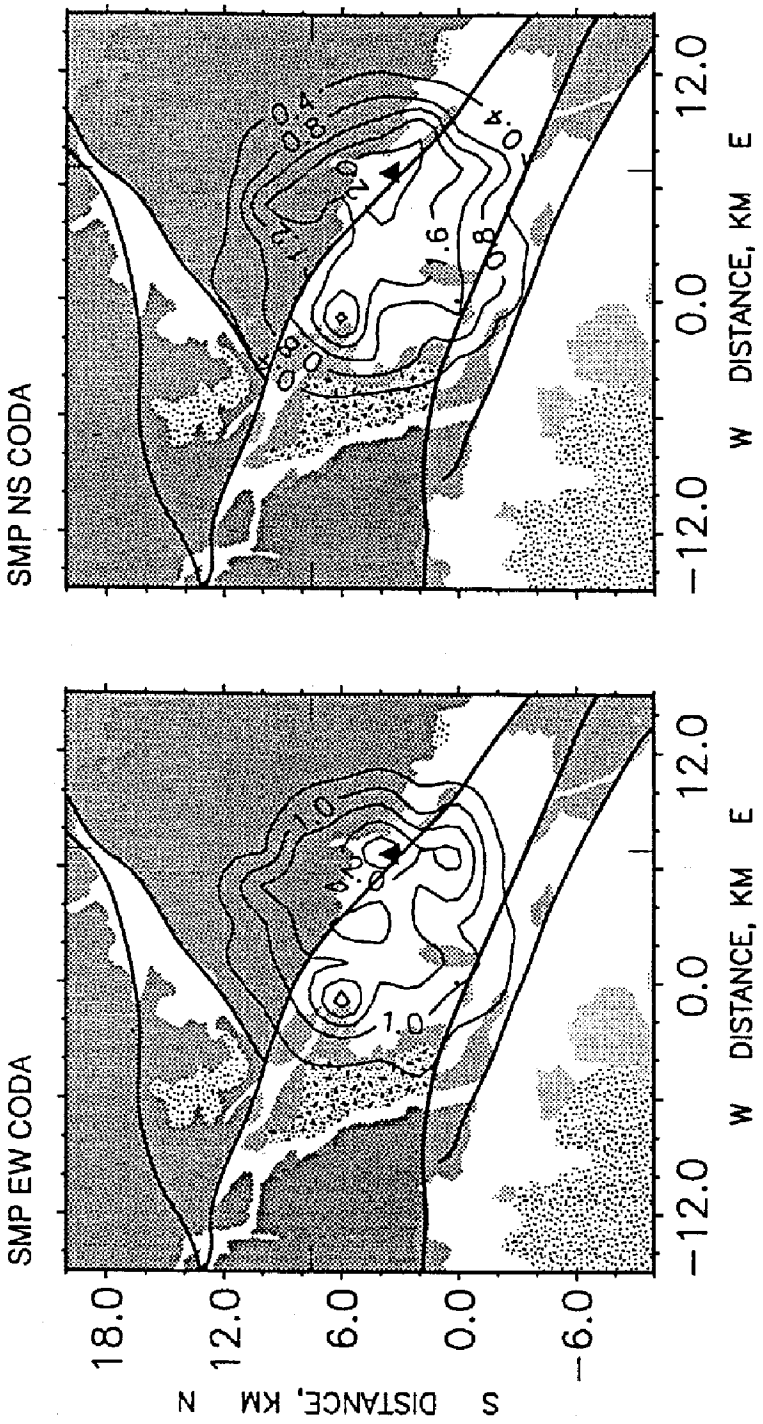

Fig. 6 SMP power distribution (contours) superimposed on the geology of the study area. Seismic data are 13 s of early coda beginning just after the direct S pulse, for the east-west (left) and north-south (right) velocity at SMP (triangle). Scatterer power in both components is peaked at point *F* (Figure 1), which is at the contact between alluvium and the Cabezon Fanglomerate. See Figure 1 for explanation of geologic units. Power units are arbitrary.

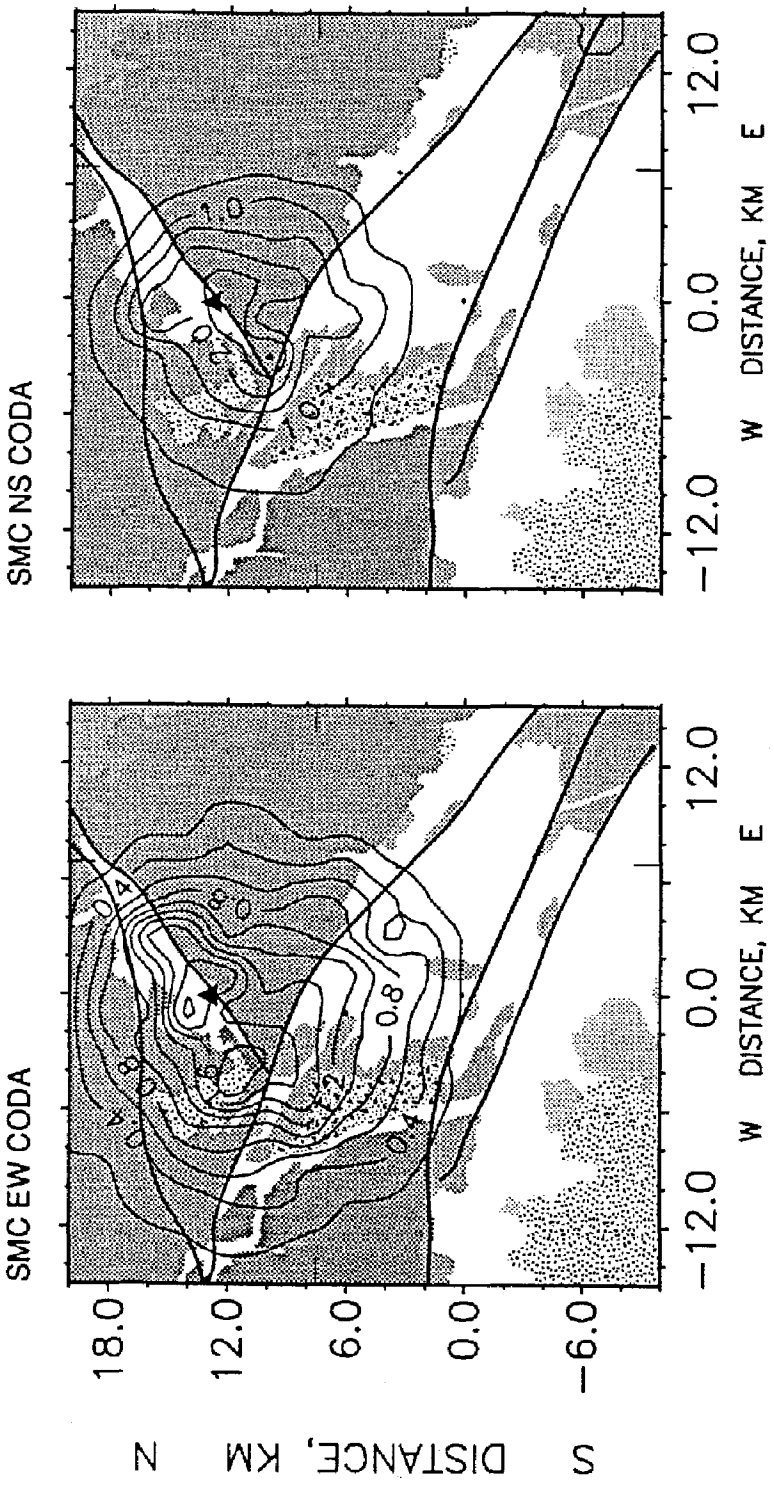

Fig. 7 SMC power distribution (contours) superimposed on the geology of the study area (from Figure 1). Seismic data are 13 s of early coda beginning just after the direct *S* pulse, for the east-west (left) and north-south (right) velocity at SMC (triangle). The power peak about 4 km southwest of SMC is denoted point *M* (see Figure 1). Power units are arbitrary.

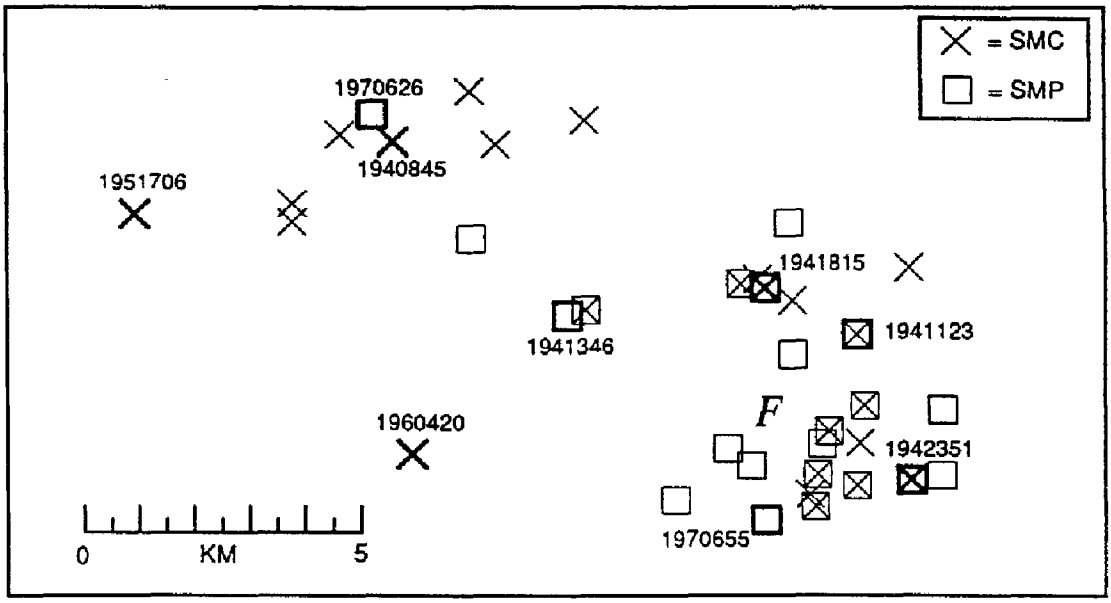

Fig. 8 Enlarged map of aftershock epicenters (X's and squares) observed at SMC and SMP, respectively. Heavy X's and squares correspond to data shown in Figures 9 and 11. Seven-digit codes near the heavy symbols are the day number (1-366) and time (UTC) used to identify the events. *F* shows the location of the strong scatterer observed in Figure 6. Aftershock zone dips northeast.

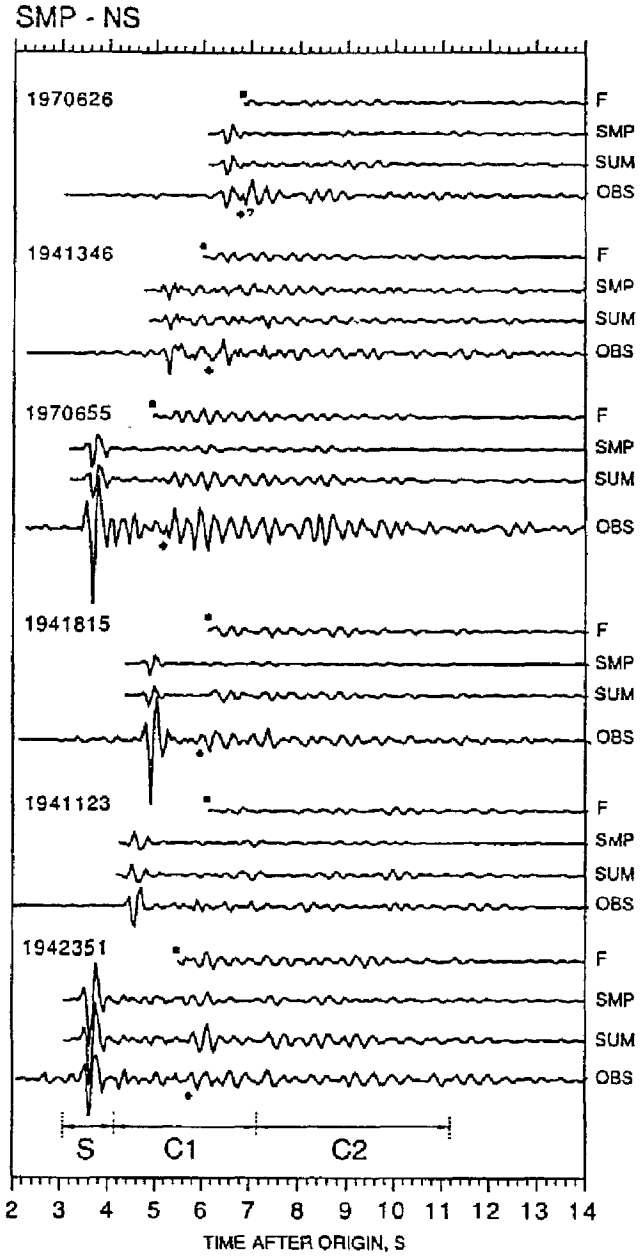

Fig. 9 Observed and predicted north-south ground motions at SMP based on a two-scatterer model of the region, for 6 aftershocks located as in Figure 9. Traces labeled 'F' are the ground motions caused by scattering from point *F* at the basin edge, 'SMP' indicates motions consisting of direct S and site reverberations modeled by the scatterer at SMP, 'SUM' is the sum of the SMP and F contributions, and 'OBS' is the observed motion. Diamonds indicate the onset of a conspicuous phase following *S* in the data, and squares indicate the arrival time of an S body wave scattered from *F* in the synthetic motions. S, C1 and C2 are three data time windows analyzed (see Figure 10).

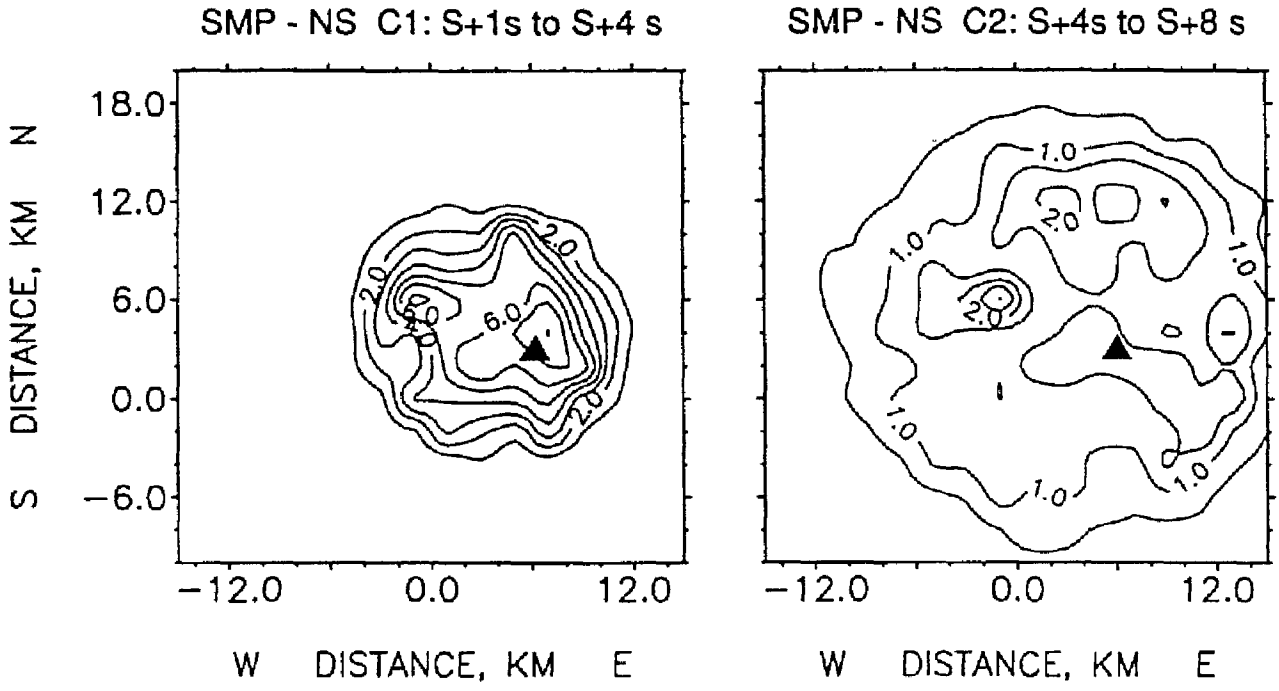

Fig. 10 Power distribution for sequential coda windows C1 and C2 in the SMP-NS data (Figure 9). Solid circle indicates point *F* and the solid triangle indicates station SMP. Note that the power peak at point *F* (circle) can be seen in both windows, indicating that waves scattered from *F* to SMP persist for several seconds. Power units are arbitrary.

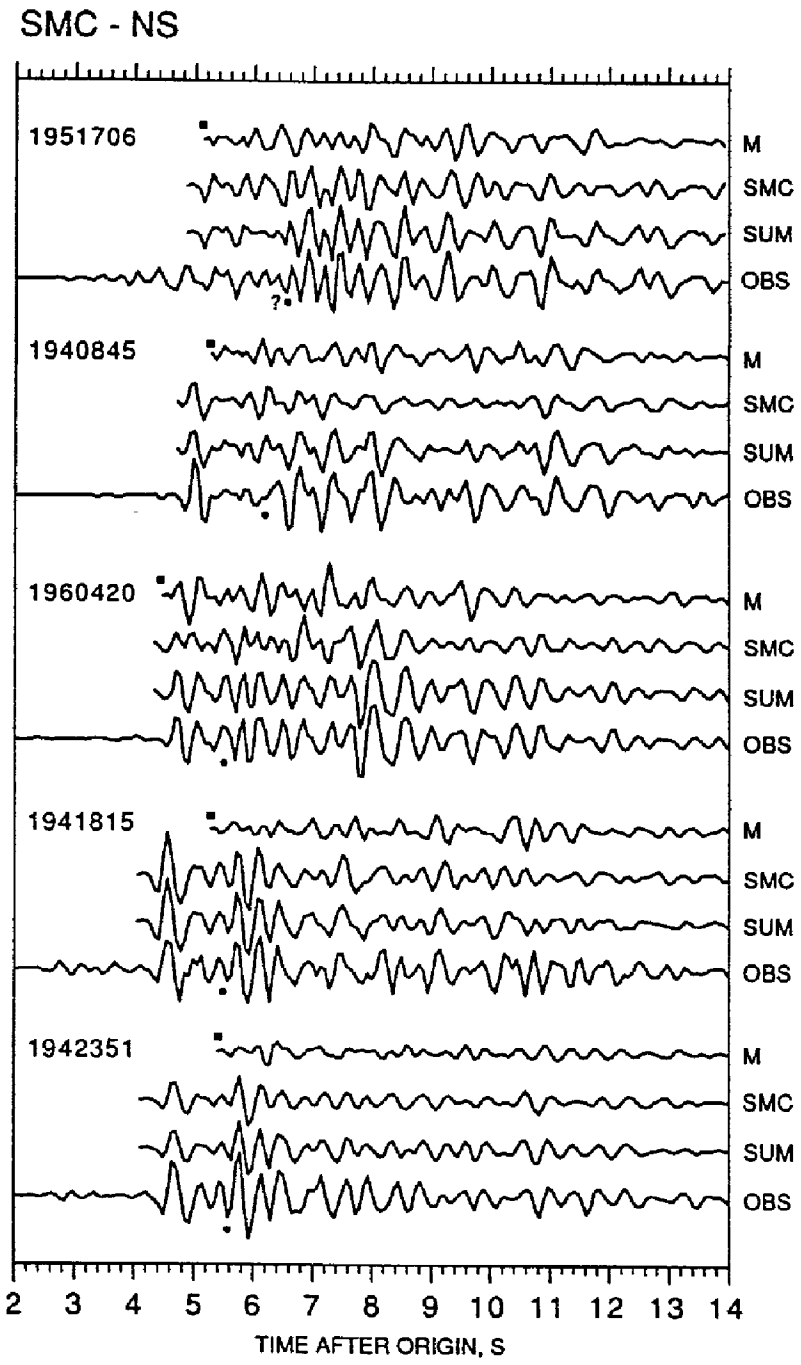

Fig. 11 Observed and predicted north-south ground motions at SMC based on a two-scatterer model of the region, for 5 aftershocks in Figure 8. Traces labeled 'M' are the ground motions caused by scattering from point *M* at the basin edge (see Figure 1), 'SMC' indicates motions consisting of direct S and site reverberations modeled by the scatterer at SMC, 'SUM' is the sum of the SMC and *M* contributions, and 'OBS' is the observed motion. Solid circles indicate the onset of a site reverberation following *S*, and squares indicate the arrival time of an S body wave scattered from *M* (such a wave is not seen in the data).

TITULOS PUBLICADOS

BASES DE DATOS PARA LA ESTIMACION DE RIESGO SISMICO EN LA CIUDAD DE MEXICO; Coordinación de Investigación; Area de Riesgos Geológicos; M. Ordaz, R. Meli, C. Montoya-Dulché, L. Sánchez y L.E. Pérez-Rocha.

TRANSPORTE, DESTINO Y TOXICIDAD DE CONSTITUYENTES QUE HACEN PELIGROSO A UN RESIDUO; Coordinación de Investigación; Area de Riesgos Químicos; Ma. E. Arcos, J. Becerril, M. Espíndola, G. Fernández y Ma. E. Navarrete.

PROCESOS FISICOQUIMICOS PARA ESTABILIZACION DE RESIDUOS PELIGROSOS; Coordinación de Investigación; Area de Riesgos Químicos; M. Y. Espíndola y G. Fernández.

REFLEXIONES SOBRE LAS INUNDACIONES EN MEXICO; Coordinación de Investigación; Area de Riesgos Hidrometeorológicos; R. Domínguez, M. Jiménez, F. García y M.A. Salas.

MODELO LLUVIA-ESCURRIMIENTO; Coordinación de Investigación; Area de Riesgos Hidrometeorológicos; R. Domínguez, M. Jiménez, F. García y M.A. Salas

REPORT ON THE JANUARY 17, 1994 NORTHRIGDE EARTHQUAKE. SEISMOLOGICAL AND ENGINEERING ASPECTS, Coordinación de Investigación; Areas de Riesgos Geológicos y de Ensayes Sísmicos; T. Mikumo, C. Gutiérrez, K. Kikuchi, S. M. Alcocer y T. A. Sánchez.

APPLICATION OF FEM (FINITE ELEMENT METHOD) TO RC (REINFORCED CONCRETE) STRUCTURES; Coordinación de Investigación; Area de Ensayes Sísmicos, H. Noguchi.

DEVELOPMENT OF ADVANCED REINFORCED CONCRETE BUILDINGS USING HIGH-STRENGTH CONCRETE AND REINFORCEMENT -NEW CONSTRUCTION TECHNOLOGY IN JAPAN-; Coordinación de Investigación; Area de Ensayes Sísmicos; S. Otani.

A STUDY ON NONLINEAR FINITE ELEMENT ANALYSIS OF CONFINED MASONRY WALLS; Coordinación de Investigación; Area de Ensayes Sísmicos; K. Ishibashi; H. Kastumata; K. Naganuma; M. Ohkubo.

SEGURIDAD SISMICA DE LA VIVIENDA ECONOMICA; Coordinación de Investigación; Area de Ensayes Sísmicos; R. Meli; S.M. Alcocer; L A. Díaz Infante; T.A. Sánchez; L.E. Flores; R. Vázquez del Mercado; R.R. Díaz.

DETERMINISTIC INVERSE APPROACHES FOR NEAR-SOURCE HIGH-FRECUENCY STRONG MOTION; Coordinación de Investigación; Area de Riesgos Geológicos; M. Iida.

SISMICIDAD Y MOVIMIENTOS FUERTES EN MEXICO: UNA VISION ACTUAL; Coordinación de Investigación; Area de Riesgos Geológicos; S. K. Singh, M. Ordaz.

JAPANESE PRESSS DESIGN GUIDELINES FOR REINFORCED CONCRETE BUILDINGS; Coordinación de Investigación; Area de Ensayes Sísmicos, S. Otani.

COMENTARIOS SOBRE LAS NORMAS INDUSTRIALES JAPONESAS DE LA CALIDAD DE AGREGADOS PARA EL CONCRETO; Coordinación de Investigación; Area de Ensayes Sísmicos; M. Saito, H. Kitajima, K. Suzuki, S. M. Alcocer.

COMENTARIOS SOBRE LAS NORMAS INDUSTRIALES JAPONESAS DE LA CALIDAD DEL CONCRETO; Coordinación de Investigación; Area de Ensayes Sísmicos; M. Saito, H Kitajima, K. Suzuki, S. M. Alcocer.

NORMAS DE DISEÑO PARA ESTRUCTURAS DE MAMPOSTERIA DEL INSTITUTO DE ARQUITECTURA DEL JAPON; Coordinación de Investigación; Area de Ensayes Sísmicos; K. Yoshimura, K. Kikuchi, T. A. Sánchez.

RED DE OBSERVACION SISMICA DEL CENAPRED, REGISTROS ACELEROGRAFICOS OBTENIDOS DURANTE 1993, Coordinación de Investigación; Area de Instrumentación Sísmica; B. López, R.Quaas, S. Medina, E. Guevara, R. González.